Key Points:
- The 2017 solar eclipse provides a unique opportunity to evaluate land-atmosphere interactions
- Comprehensive surface fluxes and boundary layer profiling observations were made at three sites during the eclipse event
- The turbulence and stability in the boundary layer evolved dramatically during the event, with time scales that depended on height

Correspondence to:
D. D. Turner,
dave.turner@noaa.gov

Response of the Land-Atmosphere System Over North-Central Oklahoma During the 2017 Eclipse

D. D. Turner[1] [iD], V. Wulfmeyer[2] [iD], A. Behrendt[2] [iD], T. A. Bonin[3] [iD], A. Choukulkar[3] [iD], R. K. Newsom[4] [iD], W. A. Brewer[5], and D. R. Cook[6] [iD]

[1]NOAA/OAR/ESRL Global Services Division, Boulder, CO, USA, [2]Institute of Physics and Meteorology, University of Hohenheim, Stuttgart, Germany, [3]Cooperative Institute for Research in Environmental Sciences, University of Colorado, Boulder, CO, USA, [4]Pacific Northwest National Laboratory, Richland, WA, USA, [5]NOAA/OAR/ESRL Physical Sciences Division, Boulder, CO, USA, [6]Argonne National Laboratory, Argonne, IL, USA

Abstract On 21 August 2017, a solar eclipse occurred over the continental United States resulting in a rapid reduction and subsequent increase of solar radiation over a large region of the country. The eclipse's effect on the land-atmosphere system is documented in unprecedented detail using a unique array of sensors deployed at three sites in north-central Oklahoma. The observations showed that turbulent fluxes of heat and momentum at the surface responded quickly to the change in solar radiation. The decrease in the sensible heat flux resulted in a decrease in the air temperature below 200 m, and a large decrease in turbulent motions throughout the boundary layer. Furthermore, the turbulent mixing in the boundary layer lagged behind the change in the surface fluxes, and this lag depended on the height above the surface. The turbulent motions increased and the convective boundary layer was reestablished as the sensible heat flux recovered.

Plain Language Summary Turbulent motions in the lower part of the atmosphere are driven strongly by the heating of the surface of the earth by the sun during the daytime. Observations during the 2017 solar eclipse provide a detailed look at how the turbulent nature of the atmosphere changed as the solar energy at the surface responded as the moon moved across the sun during the eclipse.

1. Introduction

An accurate simulation of the Earth system on any scale requires an understanding and representation of land-atmosphere (L-A) interaction and feedback processes (Dirmeyer, 2011; Santanello et al., 2017; Seneviratne et al., 2010). L-A interaction plays a crucial role in the evolution of the planetary boundary layer (PBL) (Van Driel & Jonkers, 2011; Van Heerwaarden et al., 2009), clouds (Ek & Holtslag, 2004; Phillips & Klein, 2014), convection (Gentine et al., 2013), and precipitation (Findell et al., 2011; Pielke et al., 2007). However, significant errors in the representation of L-A feedbacks are still present in almost all types of modeling systems ranging from mesoscale weather forecast models (Milovac et al., 2016) to climate models (Mei & Wang, 2012) to reanalyses (Zeng et al., 2010).

While it is clear that there are deficiencies in the chain of parameterizations of land-surface, surface-layer, and PBL turbulent processes, it has been proven to be very difficult to disentangle and identify the key problems. This challenge is amplified by a lack of observational data for determining various norms to characterize coupling strengths, which must include observations of key variables in the soil-vegetation-atmosphere system including high-resolution profiles of wind, temperature, and humidity. These studies also require the gradients in these profiles as well as their turbulent moments, fluxes such as the sensible and the latent heat, and turbulent kinetic energy (TKE) (Van Heerwaarden et al., 2009; Wulfmeyer et al., 2015, 2016).

The August 2017 eclipse event over the United States provides an excellent opportunity to evaluate the accuracy of how L-A interactions are represented in numerical models, as essentially the eclipse simulated a rapid sunset/sunrise event (Harrison & Hanna, 2017). This eclipse occurred near midday when the convective boundary layer (CBL) was already well developed and thus provides an opportunity to observe how quickly turbulent fluxes of heat and momentum decay and regenerate in response to throwing the "solar switch." We will show that during this event, the developing CBL evolved into a stable boundary layer (SBL), which became unstable again after the recovery of solar radiation.

Table 1
Information About Each of the Sites Used in the Paper

| Site name (closest town)	Latitude [°N]	Longitude [°E]	Elevation [m MSL]	Minimum DSWF [W m^{-2}]	Mean Sfc Q [g kg^{-1}]	Mean Sfc T [C]	Mean Sfc wind [m s^{-1}]	Instruments	Primary land use
E32 (Medford)	36.819	−97.820	328	56.2	15.7	32.1	5.9	AERI, DLID, SfcMet, EBBR, solar radiometers	Pasture
C1 (Lamont)	36.605	−97.485	318	84.2	14.5	31.5	7.3	AERI, DLIDx2, SfcMet, ECOR, RLID, solar radiometers	Pasture, wheat stubble, and soybeans
E39 (Morrison)	36.374	−97.069	279	86.9	16.2	31.2	6.1	AERI, DLID, SfcMet, ECOR, solar radiometers	Pasture and soybeans

Note. The closest towns to each site, all of which are in Oklahoma, are within 15 km. These sites are shown in Figure 1 as yellow (E32), red (C1), and green (E39) dots. DSWF: downwelling shortwave flux (at the surface), Sfc: surface (i.e., 2 m AGL), Q: water vapor mixing ratio, T: ambient temperature, AERI: Atmospheric Emitted Radiance Interferometer, DLID: Doppler lidar, SfcMet: surface meteorological station, EBBR: energy balance Bowen ratio station, ECOR: eddy correlation station, RLID: Raman lidar. The land use column captures the primary land use in the area surrounding each site.

We use a unique set of observations that show the evolution of the fluxes at the land surface and the resulting impact on the entire PBL at three locations across north-central Oklahoma. These observations include wind, temperature, and humidity remote sensing systems that allow the profiles of the mean and higher-order moments throughout the PBL to be investigated. These observations were collected as part of the Department of Energy Atmospheric Radiation Measurement (ARM) program (Turner & Ellingson, 2016) at its Southern Great Plains site (Sisterson et al., 2016). The ARM observations were augmented by instruments deployed as part of the Land-Atmosphere Feedback Experiment (LAFE) that was being conducted at the ARM central facility location in August 2017. Data from three sites (denoted E32, C1, and E39; locations provided in Table 1 and illustrated in Figure 1) were analyzed to investigate the spatial variability and representativeness of the observations.

2. The Eclipse

The eclipse event in north-central Oklahoma started around 1640 UTC (local time is UTC −5 h) and ended at approximately 1930 UTC. The evolution of the event is shown in the left side of Figure 1, with the maximum obscuration of the Sun occurring near 1803 UTC (about 89% blockage). During this eclipse event, the skies above our sites in north-central Oklahoma were largely cloud-free before, during, and directly after the event (Figure 1), with southerly near-surface winds. The atmosphere was relatively moist, with approximately 42 kg m^{-2} of precipitable water vapor. The sky above the three sites was cloud-free except that a layer of thin cirrus was above the E32 site just before and during the eclipse. About 1–2 h after the eclipse, a few cumulus clouds at the top of the PBL and some thin cirrus were observed at all three ARM sites.

Many different instruments were used to observe the evolution of the surface fluxes and the resulting impact on the structure and turbulence in the PBL. At each of the three sites, the downwelling shortwave radiative flux is observed using a narrow incidence pyrheliometer and a precision spectral pyranometer to measure the direct beam and diffuse irradiance, respectively, which are then algebraically combined to get the total solar downwelling flux at the surface (Michalsky & Long, 2016). Sensible and latent heat fluxes are measured using either eddy correlation or energy balance Bowen ratio stations, the choice of which was deployed depending on the land use (Berg & Lamb, 2016) (Table 1). Note that the relative accuracy of the two types of measurement systems is within 20% for most conditions (Fritschen et al., 1992). Scanning Doppler lidars (DLIDs) at all three sites are used to measure horizontal winds (every 15 min at E32 and E39) using a velocity-azimuth display method (Newsom et al., 2017) and vertical motions at 1 s resolution otherwise. The vertical motion data sets were processed to provide profiles of their variance and skewness (Berg, Newsom, & Turner, 2017), thereby providing a description of the turbulent motions in the PBL. Each site also includes an Atmospheric Emitted Radiance Interferometer (AERI) that measures downwelling spectral infrared radiance (Knuteson et al., 2004), from which profiles of temperature are retrieved (Turner & Löhnert, 2014). At the C1 facility only, the ARM program operates a Raman lidar (Turner, Goldsmith, & Ferrare, 2016) that
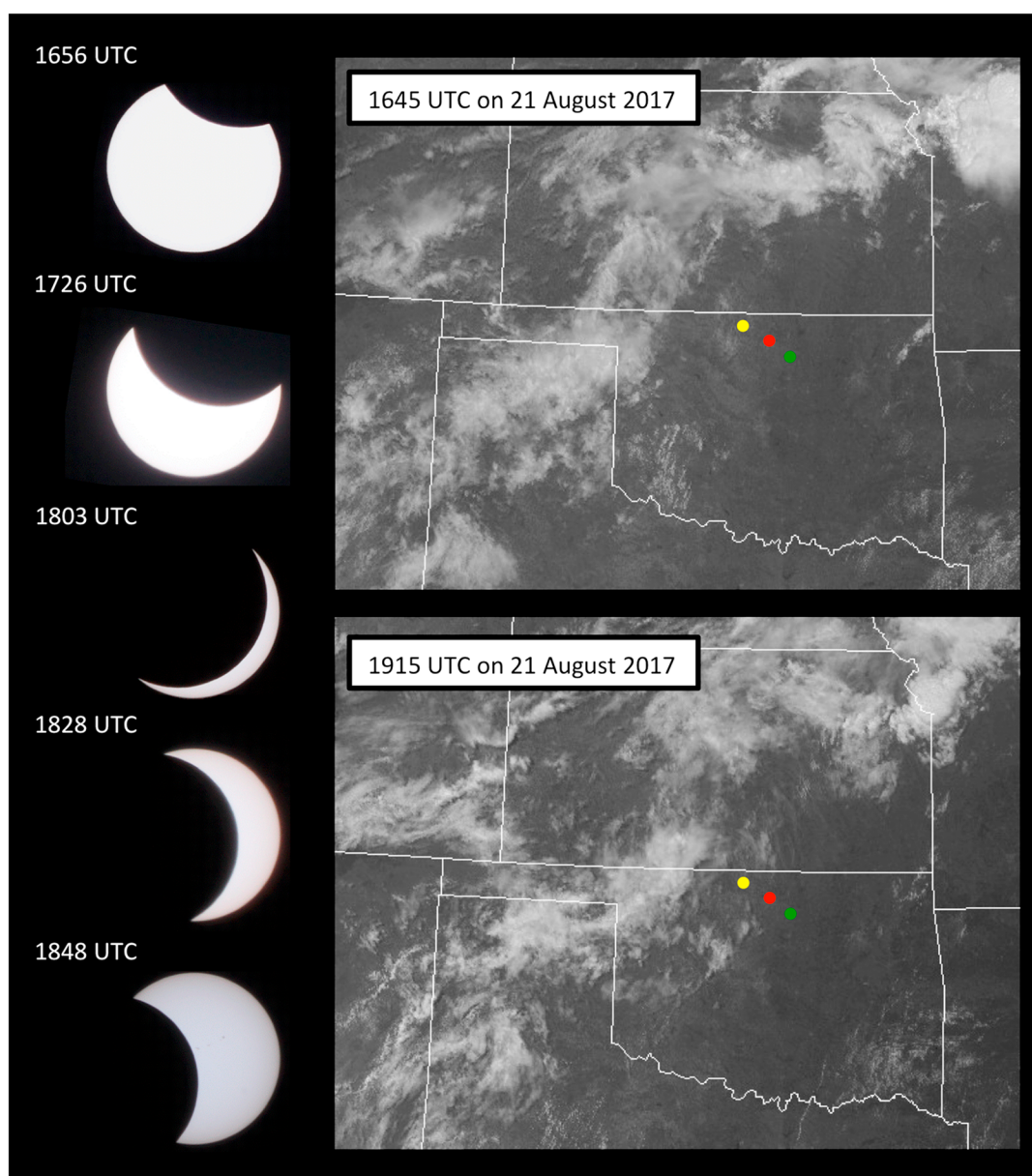
Figure 1. (left) Photos of the solar eclipse taken at the C1 site and (right) visible geostationary satellite images taken before and after the eclipse. The yellow, red, and green dots indicate the locations of the E32, C1, and E39 sites, respectively (the satellite images were downloaded from the National Center for Atmospheric Research MMM image archive at http://www2.mmm.ucar.edu/imagearchive/).

measures profiles of water vapor mixing ratio and its higher order moments (Turner et al., 2014). Additionally at the C1 facility, a second DLID from the University of Hohenheim was deployed as part of LAFE and operated in a special scanning mode from which TKE profiles were derived using the six-beam technique (Bonin et al., 2017; Sathe et al., 2015). A large number of other guest instruments were also operated at the C1 facility during LAFE to study L-A interactions, but they are not used in this analysis.

During the solar eclipse, which occurred very close to local noon in Oklahoma, the downwelling solar radiation decreased nearly 800 W m^{-2} from its normal clear-sky value. During the peak of the eclipse, approximately 85 W m^{-2} reached the surface at the C1 and E39 sites, while the E32 site received only 56 W m^{-2} due to additional attenuation from a thin overhead cloud layer observed by the AERI at that location (the signature of the cirrus can be seen in the nonsmooth nature of the solar flux observations at the E32 site in Figure 2a). This strong change in the downwelling solar radiation had an immediate impact on the surface
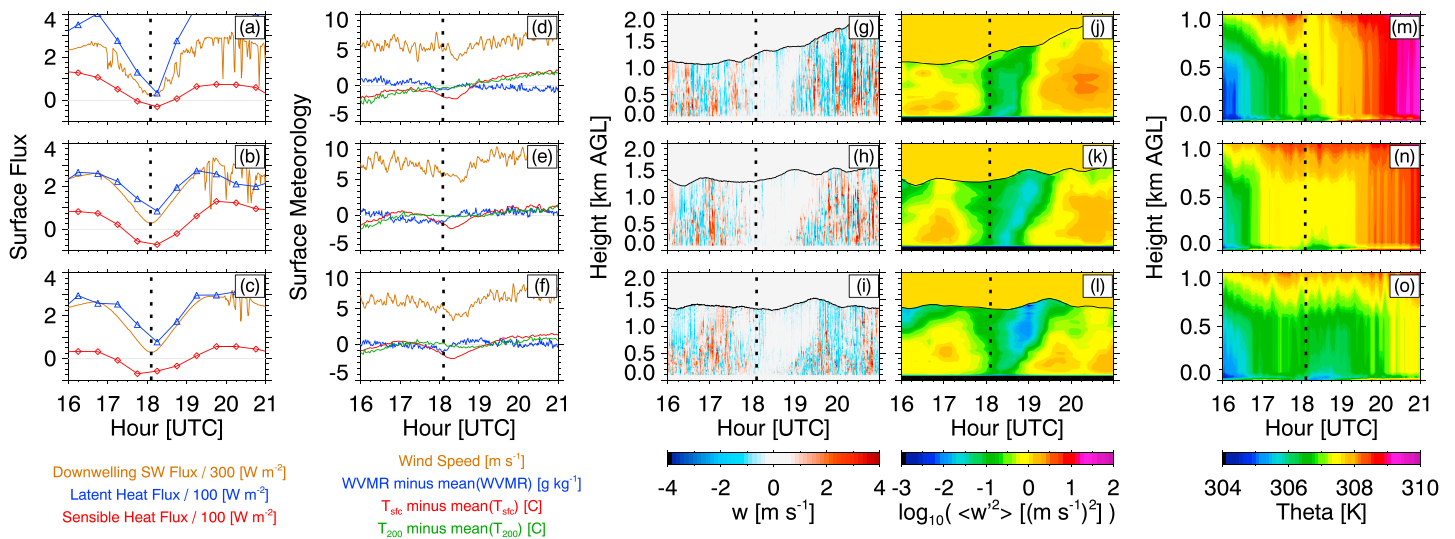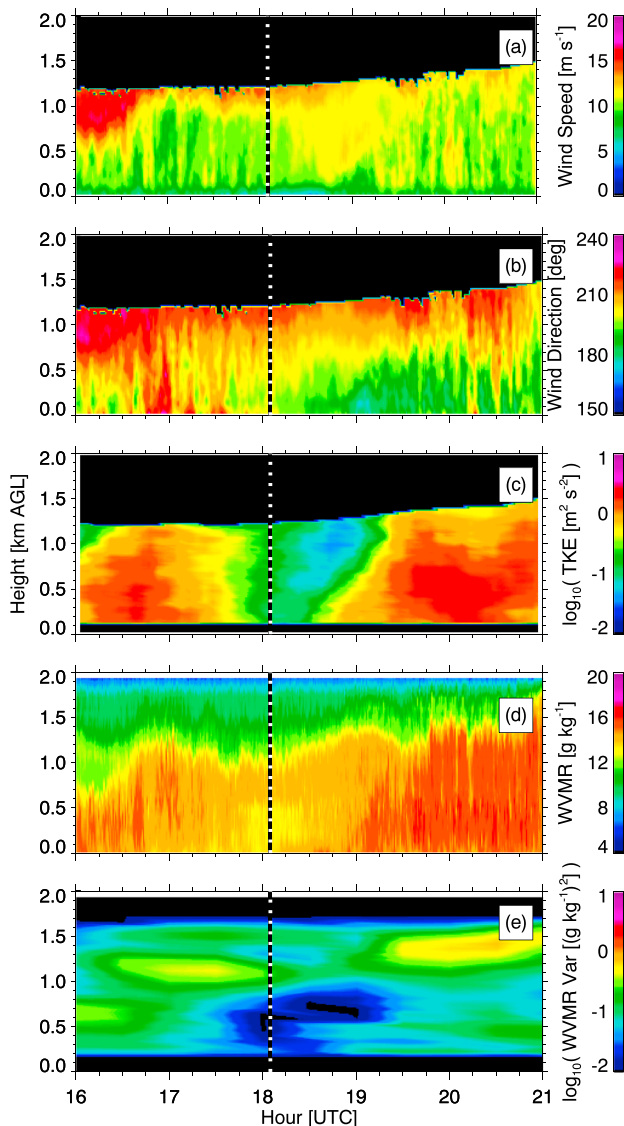
Figure 2. Observations at the SGP site on 21 August 2017 from 16:00 to 21:00 UTC. Downwelling shortwave (brown), sensible heat (red), and latent heat (blue) fluxes at the surface (a–c); 10 m wind speed (brown) and deviations of the 2 m temperature (red), 2 m water vapor mixing ratio (blue), and 200 m temperature (green) from the mean (d–f) where the mean values are given in Table 1; profiles of vertical motions at 1 s resolution (g–i); profiles of the variance (30 min resolution but calculated every 10 min) of the vertical motions (j–l); and potential temperature profiles at 5 min resolution (m–o). The top, middle, and bottom rows correspond to observations at the E32, C1, and E39 sites, respectively. The dashed vertical lines in all panels indicate the time of maximum solar eclipse. The solid black line in (g)–(l) denote the level where the lidar's signal-to-noise ratio drops below -21 dB; points above that level are very noisy and not shown. Note that (m)–(o) have a different vertical range (0 to 1 km) relative to the other time-height cross sections in (g)–(l) (0 to 2 km).

energy budget, resulting in strong decreases in both sensible and latent heat fluxes at the three sites that were correlated with the solar fluxes (Figures 2a–2c). At all three sites, the sensible heat flux was negative for at least an hour near the peak eclipse, although the latent heat fluxes remained positive throughout the event.

The change in the surface fluxes impacted the near-surface air temperature and winds (Figures 2d–2f). At all three sites, the 2 m air temperature decreased by 2–3°C and the 10 m wind speed decreased by 1–2 m s^{-1} from a mean speed of approximately 6 m s^{-1} (see Table 1 for the mean speed at each site). These decreases lagged the peak of the eclipse by 10–15 min, with slight differences among the three sites. Lags of this magnitude have been seen in other studies (Aplin, Scott, & Gray, 2017; Hanna, 2000) and are hypothesized to be due to thermal inertia of the surface layer (Aplin & Harrison, 2003). Furthermore, the variability in the 10 m winds also decreased (i.e., it was less gusty) for about 10–20 min at each site; this has also been observed during other eclipses (Eaton et al., 1997). The change in the 2 m water vapor mixing ratio observations did not seem to show any consistent picture across the three sites. Interestingly, the evolution of the temperature at 200 m (retrieved from the AERI and discussed in more detail below) does not show a decrease associated with this eclipse.

The rapid decrease in the surface sensible heat flux had a marked impact on the vertical motions throughout the PBL at all three sites (Figures 2g–2i). The magnitude of the up/down drafts decreased quickly, achieving values near zero by 1800 UTC. The vertical velocity variance profiles (Figures 2j–2l), which were computed using the Lenschow et al. (2000) technique to account for instrument noise, show that the variance decreased almost uniformly with height at the E32 site but that the rate of the decrease in variance changed with height at the C1 and E39 sites with the decrease happening at upper levels first. Like the surface meteorology observations, the minimum in the vertical velocity variance at 100 m lagged the peak eclipse by 10–15 min at all sites, but the C1 and E39 sites show that the minimum in the variance lagged behind the peak eclipse by almost an hour at 1.2 km above the ground. The increase in the surface sensible heat fluxes, which were positive at all three sites by 1900 UTC, resulted in the regeneration of the turbulent motions near the surface (Figures 2g–2i) that gradually expanded vertically over the next 45 min to the entire PBL (Figures 2j–2l). However, while the evolution in the variance profiles at the C1 and E39 sites is similar, the evolution of the variance profile at the E32 site was markedly different.

Figure 3. Profile observations at the Southern Great Plains C1 site on 21 August 2017 from 16:00 to 21:00 UTC. (a) Horizontal wind speed (1 min resolution), (b) horizontal wind direction (1 min resolution), (c) turbulent kinetic energy (15 min resolution), (d) water vapor mixing ratio (10 s resolution), and (e) water vapor mixing ratio variance (30 min resolution). The times correspond to the middle of the averaging periods.

To better understand the vertical motion variance profile at E32 relative to the other two sites, we investigated the evolution of the stability of the lowest 1 km of the PBL using potential temperature profiles derived from AERI retrievals (Figures 2m–2o). The vertical resolution of these temperature profiles retrieved from the AERI is approximately the same as the altitude above the ground; that is, 100 m at 100 m above ground level (AGL) and 1 km at 1 km AGL (Turner & Löhnert, 2014). Note that there is a small artifact at 25 m AGL in the retrieved temperature profiles that is related to an unresolved problem in the retrieval's forward model. All three locations show the development of an SBL with a shallow (no deeper than 150 m, which is confirmed by the 200 m temperature traces in Figures 2d, 2e, and 2f) inversion at the surface that started near the time of peak eclipse and persisted for about 45 min. At the C1 and E39 sites, the PBL between 50 m and 650 m (at E39) or 800 m (at C1) was largely neutrally buoyant from 1630 to 1745 UTC, and again after 1920 UTC. At the E39 site, there is a slight increase in potential temperature above 300 m from 1745 to 1920 UTC, suggesting that it became slightly more stable during the eclipse. However, the potential temperature above the C1 site for this time period is almost constant, suggesting that it remained neutrally buoyant over this height range throughout the eclipse. The E32 site showed a much different evolution of the stability of the PBL than the other two sites, with significant changes in the stability profile from 1745 to 1920 UTC. We speculate that the increase in stability with height at the E32 site is associated with a combination of the difference in the surface fluxes (relative to the other two sites) and temperature advection that occurred at the E32 site (the wind direction was from the southwest from the surface up to 1 km starting at 1845 UTC), whereas the wind profiles for the other two sites after this time were very similar and from the south (Figure 3b shows the wind direction profiles from the C1 site; horizontal wind direction profiles from the other two sites are not shown).

The additional instrumentation at the ARM central facility (C1) provided a more detailed view of the evolution of the PBL. The University of Hohenheim DLID performed constant elevation conical scans, from which 1 min horizontal wind profiles and 15 min TKE profiles were derived, while the ARM DLID collected only zenith-pointing observations. The TKE profiles were derived using the so-called "6-beam" method of Sathe et al. (2015), which has been shown to slightly underestimate the TKE by 5% to 10% relative to an anemometer (Bonin et al., 2017). The evolution of the TKE profile above the C1 site (Figure 3c) is qualitatively very similar to the vertical velocity variance at that site (Figure 2k). This similarity is not surprising since the contribution of the variance from the u' and v' components to the TKE, which is defined as TKE $= 0.5 * [<u'^2> + <v'^2> + <w'^2>]$ (where $<>$ denote Reynolds averaging), is generally small relative to the w' contribution in a convectively driven turbulent PBL.

The eclipse also influenced the high-resolution wind speed and direction profiles above the C1 site (Figures 3a and 3b). The wind direction shifts as the turbulent motions increase when the Sun comes out from behind the Moon (Figure 3b). A 25° wind shift is apparent, and this wind shift moves up with altitude as the temporal increase in TKE shifts upward with time (Figure 3c). The slight backing of the wind direction due to the effects of an eclipse was shown using numerical weather prediction models in a previous event (Gray & Harrison, 2012). The wind speed (Figure 3a) increases by ~4 m s^{-1}, where the TKE is low (i.e., between 300 and 700 m from 1800 UTC until the newly formed CBL grew into this layer); this is likely due to a reduction in the drag imposed by the diminishing turbulent motions, which is one mechanism for the development of
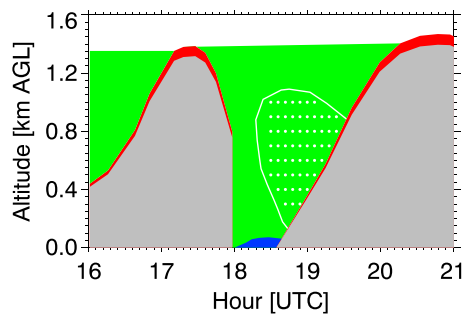
Figure 4. A conceptual diagram depicting the evolution of the convective boundary layer (gray), residual layer (green), interfacial layer (red), stable boundary layer (blue), and low-level jet (white dots with white boundary) during the eclipse event.

nocturnal low-level jet that is frequently observed over the central United States (Blackadar, 1957). As the turbulent mixing resumes near the surface at 1845 UTC and becomes deeper with time (Figures 2h and 3c), the wind speed decreases by nearly 5 m s^{-1} in the lowest 400 m (Figure 3a), which seems to support this suggestion.

The ARM C1 has an operational water vapor Raman lidar, and 10 s water vapor mixing ratio profiles are shown in Figure 3d. These observations clearly show the deepening of the moist well-mixed layer from 1600 to 1700 UTC. The Raman lidar observations then show a slight decrease in the altitude of the well-mixed layer from 1700 to 1830 UTC, after which the well-mixed layer deepens again until about 1900 UTC (Figure 3d). There are several interesting things to note about this evolution. First is the intensity of the vertical mixing, which is captured by the water vapor variance profiles (Figure 3e) and is most easily seen at the top of the PBL (between 1,200 and 1,400 m) where the water vapor gradient is largest and seems to decrease during the solar eclipse event. There is also a minimum in the water vapor variance profiles (Figure 3e) that is qualitatively well correlated with the minimum in the TKE profile (Figure 3c). (Note that we believe the slight increase in the water vapor variance between 400 and 550 m from 1830 to 1900 UTC in Figure 3e might be associated with how observations from the two fields of view of the Raman lidar are merged; the system uses two fields of view (Goldsmith et al., 1998) in order to profile water vapor from the surface to approximately 5 km.)

Second, there appears to be a slight drying of the PBL in the lowest 500 m during the middle of the eclipse event. Wingo and Knupp (2015) have shown that often there is a slight increase in the water vapor mixing ratio in the surface layer associated with the evening transition, and indeed, there is a slight increase in the surface mixing ratio near the surface after 1815 UTC (Figures 2e and 2f) that may be related to that effect. However, the in situ surface water vapor observations (Figure 2e) also suggest a slight drying from 1700 to 1815 UTC. Is this drying due to some process associated with the change in the turbulent mixing associated with the eclipse? While currently unknown, possible explanations are that the decreasing water vapor flux from the surface (Figure 2b) is not supplying enough water vapor to overcome the entrainment drying of the boundary layer at the top of the PBL or inhomogeneities in the advection of water vapor associated with the change of wind direction between 1700 and 1730 UTC below 300 m (Figure 3b).

3. Summary

In many ways, the L-A response as the Sun was obscured by the Moon was similar to the afternoon-to-evening transition (e.g., Harrison & Hanna, 2017; Wingo & Knupp, 2015), albeit much faster. The decrease in solar flux resulted in a decrease in the sensible heat flux, which caused the Earth's surface to cool with the subsequent development of an SBL with a near-surface temperature inversion. This cooling decreased the surface-driven turbulent motions in the PBL as seen in the variance of the vertical motions observed by the DLIDs (Figures 2j–2l), the TKE (Figure 3c), and the water vapor variance profiles (Figure 3e). The decrease in the turbulent mixing impacted the horizontal wind profiles, resulting in an increase of wind speed where the TKE was lowest.

However, as the Sun was only obscured for a relatively short time, the stable nocturnal-like boundary layer was only just starting to develop when the Sun emerged again from behind the Moon, thereby simulating an extremely rapid sunrise event. As the Sun reappeared, the sensible and latent heat fluxes increased with the increase in the downwelling solar radiation at the surface, causing warming of the surface and the near-surface air, thereby quickly eroding the surface inversion. The continual heating of the surface and resulting increase in the sensible heat flux generated surface-driven convective motions that reestablished a CBL that is easily identifiable in both the vertical velocity and water vapor variance. Figure 4 provides a simple representation of the evolution of the boundary layer during this event, including the decay of the CBL and its regeneration, the interfacial layer between the CBL and the atmosphere above, the development of the SBL during/after the eclipse, and the location of the low-level jet that developed in the residual layer during the event.

This event, and the observations presented here, provides an excellent opportunity to evaluate if the land-surface and PBL schemes used in numerical weather prediction and global climate models are properly capturing the L-A interactions associated with a rapid decrease/increase of solar radiation. The rapid evolution of this event, together with observations collected during normal sunrise and sunset events by the same instruments, should enable the disentanglement of the various processes at work that link the evolution of the surface properties to the evolution of the PBL. Indeed, the experimental version of the rapid refresh model (Benjamin et al., 2016), which is run operationally by the U.S. National Weather Service to provide short-to-intermediate term weather forecasts, was recently modified to include the radiative impact of an eclipse in its simulation. Work is already under way to evaluate whether this model adequately captured the evolution of the PBL during this unique event.

References

Aplin, K. L., & Harrison, R. G. (2003). Meteorological effects of the eclipse of 11th August 1999 in cloudy and clear conditions. *Proceedings of the Royal Society of London A*, *459*(2030), 353–371. https://doi.org/10.1098/rspa.2002.1042

Aplin, K. L., Scott, C. J., & Gray, S. L. (2017). Atmospheric changes from solar eclipses. *Philosophical Transactions of the Royal Society A*, *374*(2077), 20150217. https://doi.org/10.1098/rsta.2015.0217

Benjamin, S. G., Weygandt, S. S., Brown, J. M., Hu, M., Alexander, C. R., Smirnova, T. G., … Manikin, G. S. (2016). A North American hourly assimilation and model forecast cycle: The rapid refresh. *Monthly Weather Review*, *144*(4), 1669–1694. https://doi.org/10.1175/MWR-D-15-0242.1

Berg, L. K., & Lamb, P. J. (2016). Surface properties and interactions: Coupling the land and atmosphere within the ARM program. In *The atmospheric radiation measurement program: The first 20 years*, meteor. *Monograph* (Vol. 57, 57, pp. 23.1–23.17). Boston, MA: American Meteorological Society. https://doi.org/10.1175/AMSMONOGRAPHS-D-15-0044.1

Berg, L. K., Newsom, R. K., & Turner, D. D. (2017). Year-long vertical velocity statistics derived from Doppler lidar in the continental convective boundary layer. *Journal of Applied Meteorology and Climatology*, *56*(9), 2441–2454. https://doi.org/10.1175/JAMC-D-16-0359.1

Blackadar, A. K. (1957). Boundary layer wind maxima and their significance for the growth of nocturnal inversions. *Bulletin of the American Meteorological Society*, *38*, 283–290.

Bonin, T. A., Choukulkar, A., Brewer, W. A., Sandberg, S. P., Weickmann, A. M., Pichugina, Y. L., … Wolfe, D. E. (2017). Evaluation of turbulence measurement techniques from a single Doppler lidar. *Atmospheric Measurement Techniques*, *10*(8), 3021–3039. https://doi.org/10.5194/amt-10-2031-2017

Dirmeyer, P. (2011). The terrestrial segment of soil moisture-climate coupling. *Geophysical Research Letters*, *38*, L16702. https://doi.org/10.1029/2011GL048268

Eaton, F. D., Hines, J. R., Hatch, W. H., Cionco, R. M., Byers, J., Garvey, D., & Miller, D. R. (1997). Solar eclipse effects observed in the planetary boundary layer over a desert. *Boundary-Layer Meteorology*, *83*(2), 331–346. https://doi.org/10.1023/A:1000219210055

Ek, M. B., & Holtslag, A. A. M. (2004). Influence of soil moisture on boundary layer cloud development. *Journal of Hydrometeorology*, *5*(1), 86–99. https://doi.org/10.1175/1525-7541(2004)005%3C0086:IOSMOB%3E2.0.CO;2

Findell, K. L., Gentine, P., Lintner, B. R., & Kerr, C. (2011). Probability of afternoon precipitation in eastern United States and Mexico enhanced by high evaporation. *Nature Geoscience*, *4*(7), 434–439. https://doi.org/10.1038/ngeo1174

Fritschen, L. J., Qian, P., Kanemasu, E. T., Nie, D., Smith, E. A., Stewart, J. B., … Weseley, M. L. (1992). Comparisons of surface flux measurements systems used in FIFE 1989. *Journal of Geophysical Research*, *97*(D17), 18,697–18,713. https://doi.org/10.1029/91JD03042

Gentine, P., Holtslag, A. A. M., D'Andrea, F., & Ek, M. (2013). Surface and atmospheric controls on the onset of moist convection over land. *Journal of Hydrometeorology*, *14*(5), 1443–1462. https://doi.org/10.1175/JHM-D-12-0137.1

Goldsmith, J. E. M., Blair, F. H., Bisson, S. E., & Turner, D. D. (1998). Turn-key Raman lidar for profiling atmospheric water vapor, clouds, and aerosols. *Applied Optics*, *37*(21), 4979–4990. https://doi.org/10.1364/AO.37.004979

Gray, S. L., & Harrison, R. G. (2012). Diagnosing eclipse-induced wind changes. *Proceedings of the Royal Society A*, *468*(2143), 1839–1850. https://doi.org/10.1098/rspa.2012.0007

Hanna, E. (2000). Meteorological effects of the solar eclipse of 11 August 1999. *Weather*, *55*(12), 430–446. https://doi.org/10.1002/j.1477-8696.2000.tb06481.x

Harrison, R. G., & Hanna, E. (2017). The solar eclipse: A natural meteorological experiment. *Philosophical Transactions of the Royal Society A*, *374*. 20,150,225. https://doi.org/10.1098/rspa.2015.0225

Knuteson, R. O., Revercomb, H. E., Best, F. A., Ciganovich, N. C., Dedecker, R. G., Dirkx, T. P., … Tobin, D. C. (2004). The Atmospheric Emitted Radiance Interferometer. Part 1: Instrument design. *Journal of Atmospheric and Oceanic Technology*, *21*(12), 1763–1776. https://doi.org/10.1175/JTECH-1662.1

Lenschow, D. H., Wulfmeyer, V., & Senff, C. (2000). Measuring second- through fourth-order moments in noisy data. *Journal of Atmospheric and Oceanic Technology*, *17*(10), 1330–1347. https://doi.org/10.1175/1520-0426(2000)017%3C1330:MSTFOM%3E2.0.CO;2

Mei, R., & Wang, G. (2012). Summer land-atmosphere coupling strength in the United States: Comparison among observations, reanalysis data and numerical models. *Journal of Hydrometeorology*, *13*(3), 1010–1022. https://doi.org/10.1175/JHM-D-11-075.1

Michalsky, J. J., & Long, C. N. (2016). ARM solar and infrared broadband and filter radiometry. In *The Atmospheric Radiation Measurement Program: The First 20 Years*, meteor. *Monograph* (Vol. 57, 57, pp. 16.1–16.15). Boston, MA: American Meteorological Society. https://doi.org/10.1175/AMSMONOGRAPHS-D-15-0031.1

Milovac, J., Branch, O. L., Bauer, H. S., Schwitalla, T., Warrach-Sagi, K., & Wulfmeyer, V. (2016). High-resolution WRF model simulations of critical land surface-atmosphere interactions within arid and temperate climates (WRFCLIM). In W. Nagel, D. Kröner, & M. Resch (Eds.), *High performance computing in science and engineering 15: Transactions of the high performance computing center* (pp. 607–622). Heidelberg, Germany: Springer International Publishing. https://doi.org/10.1007/978-3-319-24633-8

Newsom, R. K., Brewer, W. A., Wilczak, J. M., Wolfe, D. E., Oncley, S. P., & Lindquist, J. K. (2017). Validating precision estimates in horizontal wind measurements from a Doppler lidar. *Atmospheric Measurement Techniques*, *10*(3), 1229–1240. https://doi.org/10.5194/amt-10-1229-2017

Phillips, T. J., & Klein, S. A. (2014). Land-atmosphere coupling manifested in warm-season observations on the U.S. Southern Great Plains. *Journal of Geophysical Research: Atmospheres*, *119*, 509–528. https://doi.org/10.1002/2013JD020492

Pielke, R. A. Sr., Adegoke, J., Beltran-Przekurat, A., Hiemstra, C. A., Lin, J., Nair, U. S., … Nobis, T. E. (2007). An overview of regional land-use and land-cover impacts on rainfall. *Tellus B*, *59*, 587–601.

Santanello, J. A., Dirmeyer, P. A., Ferguson, C. R., Findell, K. L., Tawfik, A. B., Berg, A., … Wulfmeyer, V. (2017). Land-atmosphere interactions: The LoCo perspective. *Bulletin of the American Meteorological Society*. https://doi.org/10.1175/BAMS-D-17-0001.1

Sathe, A., Mann, J., Vasiljevic, N., & Lea, G. (2015). A six-beam method to measure turbulence statistics using ground-based wind lidars. *Atmospheric Measurement Techniques*, *8*(2), 729–740. https://doi.org/10.5194/amt-8-729-2015

Seneviratne, S. I., Corti, T., Davin, E. L., Hirschi, M., Jaeger, E. B., Lehner, I., … Teuling, A. J. (2010). Investigating soil moisture-climate inter-actions in a changing climate: A review. *Earth-Science Reviews*, *99*(3-4), 125–161. https://doi.org/10.1016/j.earscirev.2010.02.004

Sisterson, D. L., Peppler, R. A., Cress, T. S., Lamb, P. J., & Turner, D. D. (2016). The ARM Southern Great Plains (SGP) site. In *The Atmospheric Radiation Measurement Program: The first 20 years*, *meteor. Monograph*, (Vol. 57, 57, pp. 6.1–6.14). Boston, MA: American Meteorological Society. https://doi.org/10.1175/AMSMONOGRAPHS-D-16-0004.1

Turner, D. D., & Ellingson, R. G. (Eds) (2016). *The Atmospheric Radiation Measurement (ARM) Program: The first 20 years*, *Meteor. Monograph* (Vol. 57). Boston, MA: American Meteorological Society.

Turner, D. D., Goldsmith, J. E. M., & Ferrare, R. A. (2016). Development and applications of the ARM Raman lidar. In *The Atmospheric Radiation Measurement Program: The first 20 years*, *meteor. Monograph* (Vol. 57, 57, pp. 18.1–18.15). Boston, MA: American Meteorological Society. https://doi.org/10.1175/AMSMONOGRAPHS-D-15-0026.1

Turner, D. D., & Löhnert, U. (2014). Information content and uncertainties in thermodynamic profiles and liquid cloud properties retrieved from the ground-based Atmospheric Emitted Radiance Interferometer (AERI). *Journal of Applied Meteorology and Climatology*, *53*(3), 752–771. https://doi.org/10.1175/JAMC-D-13-0126.1

Turner, D. D., Wulfmeyer, V., Berg, L. K., & Schween, J. H. (2014). Water vapor turbulence profiles in stationary continental convective boundary layers. *Journal of Geophysical Research: Atmospheres*, *119*, 11,151–11,165. https://doi.org/10.1002/2014JD022202

Van Heerwaarden, C. C., Vilà-Guerau de Arellano, J., Moene, A. F., & Holtslag, A. A. M. (2009). Interactions between dry-air entrainment, surface evaporation and convective boundary-layer development. *Quarterly Journal of the Royal Meteorological Society*, *135*(642), 1277–1291. https://doi.org/10.1002/qj.431

Van Driel, R., & Jonkers, H. J. J. (2011). Convective boundary layers driven by nonstationary surface heat fluxes. *Journal of the Atmospheric Sciences*, *68*(4), 727–738. https://doi.org/10.1175/2010JAS3643.1

Wingo, S. M., & Knupp, K. R. (2015). Multi-platform observations characterizing the afternoon-to-evening transition of the planetary boundary layer in northern Alabama, USA. *Boundary-Layer Meteorology*, *155*(1), 29–53. https://doi.org/10.1007/s10546-014-9988-1

Wulfmeyer, V., Hardesty, R. M., Turner, D. D., Behrendt, A., Cadeddu, M., Di Girolamo, P., … Zus, F. (2015). A review of the remote sensing of lower-tropospheric thermodynamic profiles and its indispensible role for the understanding and simulation of water and energy cycles. *Reviews of Geophysics*, *53*, 819–895. https://doi.org/10.1002/2014RG000476

Wulfmeyer, V., Muppa, S. K., Behrendt, A., Hammann, E., Spaeth, F., Sorbjan, Z., … Hardesty, R. M. (2016). Determination of convective boundary layer entrainment fluxes, dissipation rates, and the molecular destruction of variances: Theoretical description and a strategy for its confirmation with a novel lidar system synergy. *Journal of the Atmospheric Sciences*, *73*(2), 667–692. https://doi.org/10.1175/JAS-D-14-0392.1

Zeng, X., Barlange, M., Castro, C., & Fling, K. (2010). Comparison of land-precipitation coupling strength using observations and models. *Journal of Hydrometeorology*, *11*(4), 979–994. https://doi.org/10.1175/2010JHM1226.1